

Spectral reflectometry characterization of an extreme ultraviolet attenuated phase-shifting mask blank

Tao Shen,^{a,*} Iacopo Mochi,^a Dongmin Jeong,^{b,c} Elisabeth Mueller,^d
Paolo Ansuinelli,^a Jinho Ahn,^{b,c} and Yasin Ekinci^a

^aPaul Scherrer Institute, Laboratory for X-Ray Nanoscience and Technologies, Villigen PSI, Switzerland

^bHanyang University, Division of Materials Science and Engineering, Seoul, Republic of Korea

^cHanyang University, Industry University Collaboration Center, Seoul, Republic of Korea

^dPaul Scherrer Institute, Laboratory of Nanoscale Biology, Villigen PSI, Switzerland

ABSTRACT. **Background:** Extreme ultraviolet (EUV) attenuated phase-shifting masks are complex structures with stringent requirements for manufacturing precision and materials properties, and they have been object of extensive research lately.

Aim: We aim to characterize the optical constants (n and k) and the thickness of the layers in the mask stack with a nondestructive method.

Approach: Using a spectral reflectometry approach with EUV and soft X-ray illumination at various incidence angles, different layer's properties in a photomask blank can be selectively probed. The optical constants and the thicknesses of the layers can be obtained by fitting a suitable model to the experimental reflectance.

Results: The optical constants of the Pt-W alloy absorber and the thicknesses of the top three layers of the sample stack were accurately characterized.

Conclusions: Stacked layer's properties can be selectively probed with the instrument (REGINE) we developed. The properties of the topmost layer can be characterized by assessing the probing depth, before investigating deeper layers with a suitable choice of illumination wavelength and angle of incidence.

© The Authors. Published by SPIE under a Creative Commons Attribution 4.0 International License. Distribution or reproduction of this work in whole or in part requires full attribution of the original publication, including its DOI. [DOI: [10.1117/1.JMM.23.4.041402](https://doi.org/10.1117/1.JMM.23.4.041402)]

Keywords: spectral reflectometry; thin-film characterization; optical constants determination; extreme ultraviolet attenuated phase-shifting mask

Paper 24015SS received Mar. 30, 2024; revised May 23, 2024; accepted May 28, 2024; published Jul. 12, 2024; corrected Jul. 25, 2024.

1 Introduction

In the ever-advancing realm of semiconductor fabrication, extreme ultraviolet lithography (EUVL) has emerged as the lead technology, promising to drive the semiconductor industry toward smaller, faster, and more energy-efficient electronic devices.¹ EUVL, with its exceptionally short wavelength of 13.5 nm, offers the capability to create nanoscale features with unparalleled precision.^{2,3} To ensure the quality and reliability of the semiconductor devices, strict quality control measures and precise metrology are important throughout the fabrication process.^{4,5}

Nondestructive nanometrology is a fundamental tool for semiconductor device manufacturing. Practically, a combination of several techniques is needed throughout the fabrication

*Address all correspondence to Tao Shen, tao.shen@psi.ch

process, from EUV photomask inspection to patterned wafer metrology. EUV light not only facilitates the production of smaller features in lithography but also emerges as a powerful approach for the metrology required to characterize and analyze these intricate features in future technology nodes, thanks to its short wavelength, relevant penetration depth, and high reflectivity with relatively high grazing angles compared to that of hard X-ray.

EUV reflectometry and scatterometry stand out as powerful techniques for the metrology of thin films and periodic structures with nondestructive approaches.^{6–8} As a widely used technique for probing the properties of thin films, EUV reflectometry offers a comprehensive suite of capabilities ranging from reflectance measurement and layer thickness determination⁹ to the detailed analysis of multilayer interfaces¹⁰ and the precise extraction of optical constants,^{11–13} notably the refractive index (n), and the extinction coefficient (k).

In this study, we introduce the reflective grazing incidence nanoscope for EUV (REGINE) instrument, which is designed for EUV reflectometry, scatterometry, and coherent diffraction imaging (CDI),^{14–16} and we illustrate its application to the optical constants determination and layer thickness characterization for an EUV attenuated phase-shifting mask blank. We first use REGINE to selectively probe only the top layer of the sample stack and perform a spectral characterization of the absorber material's optical constants. Then, we increase the grazing incidence angle and use higher photon energy to probe deeper layers to study their thickness.

2 Materials and Methods

2.1 Experimental Setup and Sample Stack Model

REGINE is a synchrotron-based instrument that is designed for thin film and grating characterization as well as for CDI of patterned wafers. It is enclosed in a high vacuum chamber that operates at the pressure of 10^{-7} mbar. The main components of REGINE are illustrated in Fig. 1.

REGINE is hosted at the metrology branch of the XIL-II beamline of the Swiss Light Source (SLS). The branch is equipped with a spherical grating monochromator with a grating included angle of 170 deg and grating constant of 400 1/mm. The monochromator's spectral bandwidth is $\lambda/\Delta\lambda = 1500$ at a wavelength $\lambda = 13.5$ nm. The EUV illumination beam exiting the monochromator has a measured photon flux of 1.03×10^{12} photon/s when it reaches the $\varnothing 1$ mm entrance aperture of REGINE, then it is focused by a ruthenium-coated ellipsoidal mirror onto the surface of a vertically mounted sample. The mirror has a reflectance of 93% for 13.5 nm wavelength at

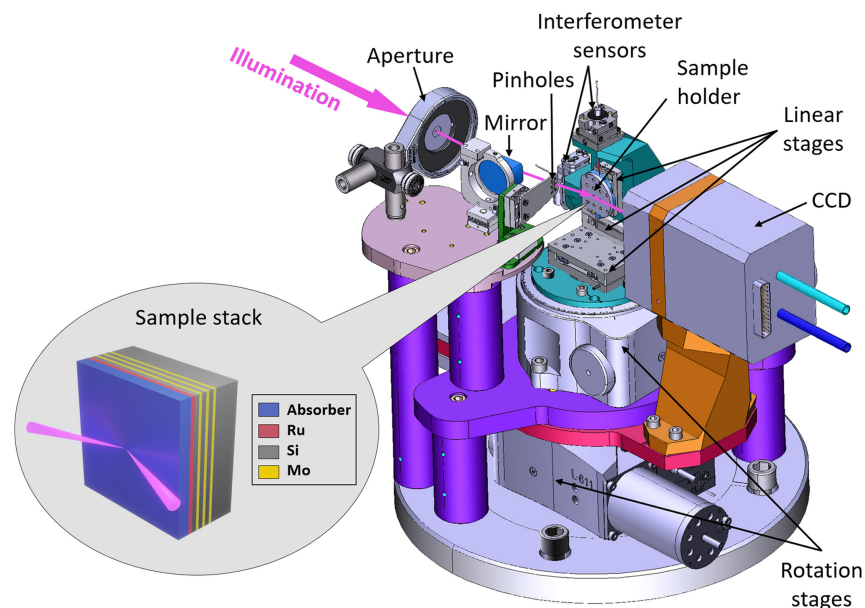


Fig. 1 3D model of the main components of REGINE. The detail shows the EUV photomask sample stack, which consists of a nonpatterned absorber layer, Ru capping layer, and 40 pairs of Si/Mo layers and Si substrate.

the grazing incidence angle of 6 deg. The sample is installed on an XYZ linear-stage set. The stage set is mounted on a rotational stage that is used to change the incidence angle of the illumination beam. The in-vacuum CCD camera (Teledyne PI-MTE2) is mounted on another co-axially installed stage, which rotates to capture the corresponding reflected light from the sample. REGINE can work in a photon energy range spanning from 80 to 200 eV, and the sample can be illuminated at a grazing incidence angle ranging from 0 deg to 28.6 deg with a p-polarized beam. Ptychography,¹⁷ the chosen CDI approach for REGINE, relies on the accurate measurement of the relative position between the illumination spot and the sample.¹⁸ To minimize the reconstruction artifacts resulting from scan position uncertainty, we have also installed two interferometric sensors to monitor the X and Y positions of the sample stage with subnanometer precision.

The structure of the sample used in this study is illustrated in the inset of Fig. 1. Its designed configuration includes a 33 nm nonpatterned Pt-W alloy absorber layer,¹⁹ a 2.5 nm Ru capping layer, and 40 bilayers of Si (4.2 nm)/Mo (2.8 nm) on a Si substrate. The sample has an area of 20 mm \times 20 mm.

In this study, we aim to obtain accurate optical constants of the absorber material, and the layer thicknesses in the sample stack. We retrieve the characteristics of the sample by calculating the reflectance with a model of the sample and then fitting it to the measurements obtained with REGINE. For this approach to yield reliable results, we require a detailed model of the sample. So we decided to perform scanning transmission electron microscopy (STEM) measurements to verify the accuracy of the sample design layout. The STEM measurements revealed the presence of intermixing layers between Ru and Si, as well as Si and Mo, which we included in our model.

Figure 2 shows the STEM image of a section of the Si/Mo multilayer, where we can observe the intermixing layer of MoSi₂ between the silicon and molybdenum layers.²⁰ To estimate the thickness of the different layers, we integrated the pixel intensities of each column of the STEM image and fitted a trapezoidal curve to the intensity distribution. We estimated the thicknesses of Si, Mo, MoSi₂ (grown on top of Si), MoSi₂ (grown on top of Mo) as 1.86 ± 0.30 , 1.94 ± 0.28 , 1.80 ± 0.29 , and 1.69 ± 0.30 nm, respectively. Based on the STEM image, the thicknesses of the absorber, Ru, and Ru-Si intermixing layers (Ru₂Si₃)²¹ were estimated by detecting the layer edges. We started by visually estimating the approximate positions of the layers' edges and for each column in the image, we extracted a vertical intensity profile centered on the edge position. Then, we fitted a fourth degree polynomial to the profile and estimated the position of the edge as

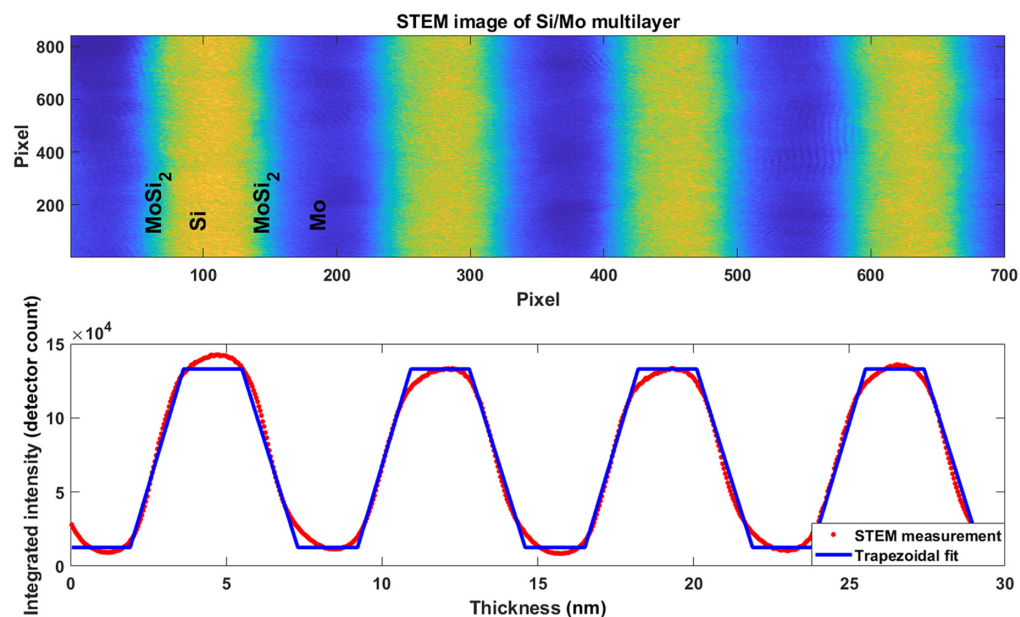


Fig. 2 STEM image of the Si/Mo multilayer and the trapezoidal fit of the integrated intensity distribution of each column. The peak and valley of the trapezoidal curve correspond to Si and Mo, respectively, and the rising and falling parts are the MoSi₂ intermixing layers.

the location corresponding to the mean of the maximum and minimum intensity values. It is important to stress that this is an arbitrary choice, and a different threshold would yield a different edge location. The estimated layer thickness was calculated as the mean value of the difference between the two layers' edges. The thicknesses of the absorber, Ru, and Ru₂Si₃ layers are 37.53 ± 0.25 , 2.48 ± 0.37 , and 1.53 ± 0.38 nm, respectively. The uncertainty was estimated as the standard deviation of the layer thickness. Due to the presence of intermixing layers, STEM provides estimated layer thicknesses based on the chosen arbitrary threshold, whereas REGINE measures the effective layer thicknesses within the range estimated by STEM.

In the photon energy range that REGINE can access, the complex refractive index (\tilde{N}) of the materials in the sample model is defined in Eq. (1) with the negative sign convention. In the initial sample model, we used the absorber n and k values provided by collaborators who developed the sample, whereas other materials' optical constants were obtained from the CXRO database:²²

$$\tilde{N}(\lambda) = n(\lambda) - i \cdot k(\lambda), \quad (1)$$

where n is the refractive index, k is the extinction coefficient, and λ is the illumination wavelength.

2.2 Reflectance Measurements

Here we describe the reflectometry experiments that we performed to determine the reflectance of the sample stack. We conducted the measurements with seven illumination wavelengths (specifically 8, 9, 10, 11.5, 12.5, 13.5, and 14.5 nm) as well as ten grazing incidence angles between 2.6 deg and 28.6 deg. The experimental geometries for data and reference collection are shown in Fig. 3.

For each of the illumination wavelengths, the sample reflectance measurements began with the collection of reference images. In this step, we moved the sample out of the beam path, allowing the illumination beam to travel directly toward the CCD. We then collected reference images with different exposure times. References were collected both before and after the data image collection to monitor the beam intensity stability. During the data image collection, the sample was moved into the beam path, and the CCD was rotated to record the reflected light from the sample, as depicted in Fig. 3. We collected images at a specific incidence angle with the same exposure times as the reference, then we rotated the sample to change the incidence angle and repeated the same procedure. This process was performed at three different positions near the center of the sample surface and the results were averaged to reduce the impact of the surface's local nonuniformity.

REGINE operates with critical illumination, where the light source is directly imaged onto the sample, and in the presence of a uniform sample, REGINE projects an Airy pattern on the detector plane. For each reference and data image set, we selected the nonsaturated image with the largest exposure time and cropped it to the size of 21×21 pixels centered on the intensity maximum, as shown in Fig. 4(a). Since the CCD has a nonlinear response at the extremes of the

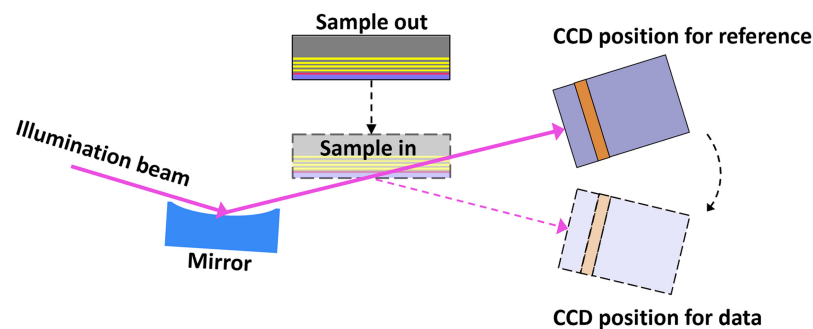


Fig. 3 Sketch of the top view of REGINE. During the reference image collection, the sample is out of the beam path, and the CCD records the beam directly from the mirror. During data image collection, the sample is moved into the beam path, and the CCD is rotated to collect the reflected beam from the sample. During the data image collection, the sample is rotated to change the grazing incidence angle and is also vertically moved to change the illuminated position.

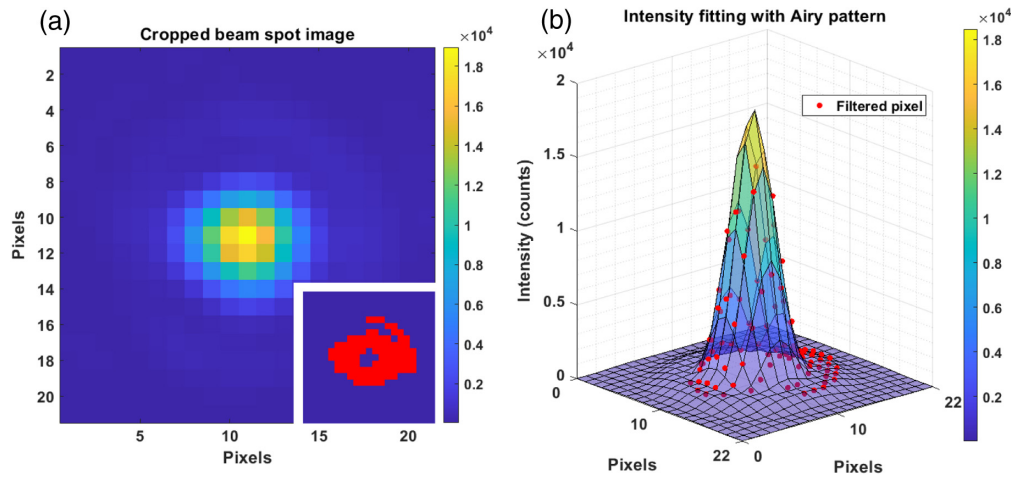


Fig. 4 (a) Beam spot data image and the intensity map created by the thresholds (inset). (b) Fitted Airy pattern and the pixels filtered by the intensity map that are used for the fitting procedure (red dots). This data image is obtained from the 13.5 nm illumination wavelength at the grazing incidence angle of 16.6 deg.

detectable intensity range, using the cropped data and reference images directly to calculate the reflectance (ratio of the two maxima) could lead to inaccurate results. For instance, at the smallest grazing incidence angle (2.6 deg), the sample reflectance calculated this way often exceeds 1. Especially in the reference images, the maximum intensity often falls within the CCD's nonlinear response range, and the readout value of the CCD is smaller than the actual intensity, resulting in a larger reflectance value. To address this issue, we applied a threshold to filter the image and used only the pixels with intensity in the CCD's linear response range for the subsequent fitting procedure. The threshold created an intensity map corresponding to the useful pixels, as shown in the inset of Fig. 4(a). We then fitted an Airy pattern function to the filtered pixels' intensity, as shown in Fig. 4(b). This procedure was applied to both data and reference images. The reflectance of the sample was calculated as the ratio of the fitted Airy function's maxima of the data and the reference.

2.3 Simulation of Reflectance and Probing Depth

In order to study the optical constants and the thickness of layers in the stack, we calculated the expected sample reflectance using the transfer matrix method (TMM)²³ for each combination of wavelength and incidence angle and compared it with the experimental results. In the simulation, the reflectance (R) of the whole sample stack is calculated as the square of the reflection coefficient (r) shown in the following equations:

$$R = |r|^2, \quad (2)$$

$$r = \frac{\gamma_0 \cdot m_{11} + \gamma_0 \cdot \gamma_s \cdot m_{12} - m_{21} - \gamma_s \cdot m_{22}}{\gamma_0 \cdot m_{11} + \gamma_0 \cdot \gamma_s \cdot m_{12} + m_{21} + \gamma_s \cdot m_{22}}, \quad (3)$$

$$M = M_1 M_2 \cdots M_n = \begin{bmatrix} m_{11} & m_{12} \\ m_{21} & m_{22} \end{bmatrix}, \quad (4)$$

where the characteristic matrix of the entire n -layer sample system (M) is the product of the individual matrices of each layer ($M_{1,2,\dots,n}$), whose elements are functions of each layer's complex refractive index, thickness, and incidence angle at the layer interface. γ_0 and γ_s are the parameters depending on the refractive index and incidence angle or refractive angle for incidence medium and substrate, respectively.

To study the illumination beam penetration in the sample stack, we also recorded the transmittance at each interface inside the stack in the simulation. When the transmittance drops below the arbitrary threshold of $1/e^2$, the light reflected by the last interface that reaches the surface of the sample is less than 1.8% of the incident intensity. Lower intensity fractions would affect the

estimated reflectance negligibly. We used this threshold to estimate the probing depth of the incident beam.

As the beam enters the absorber, we calculate the transmittance using the Fresnel equation for p-polarized light [Eqs. (5) and (6)].²⁴ Then we use the Beer–Lambert law and the specified threshold ($1/e^2$) to calculate the probing depth (d) as shown in Eqs. (7)–(9). In case the beam penetrates deeper into the sample, we simply estimate the probing depth as the sum of the layers thickness until the transmittance drops below the specified threshold at a certain interface. The reflectance R and the transmittance T of a p-polarized beam are expressed as

$$R = \left| \frac{n_1 \cdot \cos \theta_t - n_2 \cdot \cos \theta_i}{n_1 \cdot \cos \theta_t + n_2 \cdot \cos \theta_i} \right|^2, \quad (5)$$

$$T = 1 - R, \quad (6)$$

where n_1 and n_2 are the refractive indices of the incident and refractive medium, θ_i and θ_t are the incident and refractive angles, respectively. The beam intensity after propagating a distance of x is given by

$$I = I_0 \cdot T \cdot e^{-\alpha x}, \quad (7)$$

where I_0 is the intensity of the illumination beam, and the attenuation coefficient α is a function of the wavelength λ and the medium extinction coefficient k :

$$\alpha = \frac{4\pi k}{\lambda}. \quad (8)$$

Considering a maximum attenuation of $1/e^2$, the probing depth d is expressed as

$$d = -\frac{\lambda}{4\pi k} \cdot \ln \frac{1}{T e^2} \cdot \cos \theta_t. \quad (9)$$

2.4 Optimization of Complex Refractive Index and Layer Thickness

In the optimization procedure, we first built the initial model of the sample as described in Sec. 2.1, then we used the approach outlined in Sec. 2.3 to simulate the reflectance of the model and we calculated the beam probing depth under the same illumination conditions (wavelength and incidence angle) used in the experiments. We then compared the simulated reflectance with the experimental one to optimize the model parameters. The probing depth serves as the criteria for selecting suitable illumination conditions to probe a specific layer.

The probing depth based on the initial sample model is shown in Fig. 5(a). Initially, we selected illumination conditions under which the beam is only probing less than half of the absorber thickness (data points with star markers). In this case, the n and k values of the absorber's complex refractive index have the most significant impact on the sample reflectance. We then used a direct-search method²⁵ to find the n and k values that minimize the root-mean-square (RMS) difference between the reflectance predicted by the model and the measured one. After obtaining the optimal n and k values of the absorber layer, we updated the sample model and calculated the probing depth again as shown in Fig. 5(b). Based on the new probing depth result, we can select the illumination conditions, where the beam probes deeper layers beyond the absorber (data points with red circle). This allowed us to measure the thickness of the deeper layers. As these data points are not deep enough to infer the Si/Mo multilayer structure, we only used them for the characterization of the absorber, Ru, and Ru₂Si₃ layer thicknesses. In Fig. 5, when the grazing incidence angle increases from 2.6 deg to 28.6 deg, the probing depth of 9 nm illumination becomes deeper than the adjacent wavelengths, which is due to the longer attenuation length of Pt at this wavelength. Pt is the dominant element in the Pt-W absorber, and within the experimental wavelength range, it has the longest attenuation length at 8.85 nm wavelength according to the CXRO database.²²

3 Results and Discussions

In Fig. 5(a), we expected the data points with star markers to remain in the absorber layer after the n and k optimization in the simulation, and the results shown in Fig. 5(b) confirmed that.

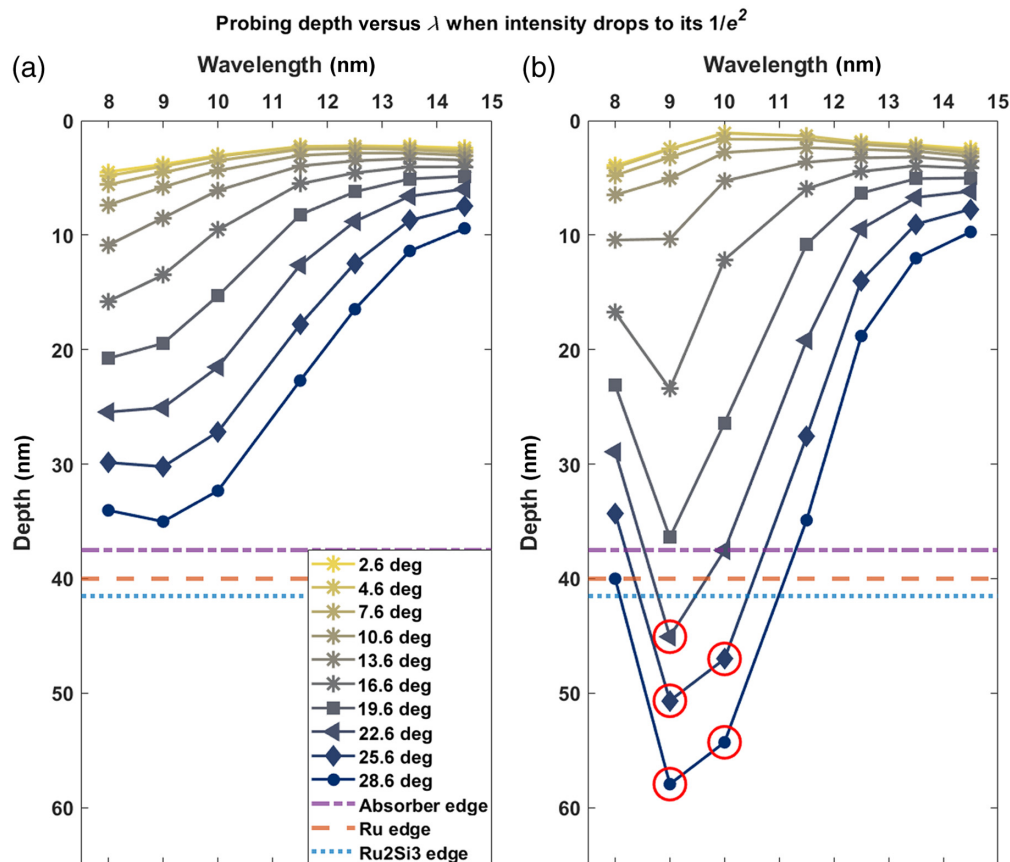


Fig. 5 Calculated probing depth when the intensity of the incident beam drops by a factor of e^2 with the sample layer thicknesses analyzed in Sec. 2.1. (a) Results with the initial absorber n and k values. (b) Results with the characterized absorber n and k values according to Sec. 2.4. The data points with red circles locate in the multilayer region and are used for thickness characterization.

Therefore, for all the wavelengths in the experiment, the intensity of the incident beam with the grazing incidence angles smaller or equal to 16.6 deg drops by a factor of e^2 within the absorber layer. These combinations of wavelength and incidence angle are used in the absorber n and k optimization procedure.

The complex refractive index of a material depends on the illumination wavelength, as shown in Eq. (1). Figure 6 shows the result of absorber n and k optimization at each wavelength. We used the initial values as the starting point to define the direct-search range with a $\pm 100\%$ variation, 1% step size for both n and k . Then, we narrowed the search range for n to $\pm 1.6\%$ of the initial value, with a step size of 0.02%, and the search range of k to $\pm 56\%$ with a step size of 0.1% (colored areas in Fig. 6). The different range and step size are due to the different magnitudes of the n and k values. The optimal values for each of the wavelengths are marked with circles in Fig. 6 within their own optimization range. The corresponding simulated sample reflectance versus experimental result is shown in Fig. 7. The optimal absorber complex refractive index was found by minimizing the RMS of the difference between the reflectance values obtained from the model and the experiment. Therefore, with the procedure described in Sec. 2.4, we can characterize the n and k values of different materials with the appropriate choice of illumination wavelengths and grazing incidence angles.

After the characterization of the n and k values for the absorber layer, we observed that the probing depth obtained with a wavelength of 9 nm and grazing incidence angles between 22.6 deg and 28.6 deg, as well as with a wavelength of 10 nm and grazing incidence angles between 25.6 deg and 28.6 deg [data points with a red circle in Fig. 5(b) are beyond the Ru_2Si_3 layer edge]. Therefore, we selected these wavelengths and incidence angles to extract

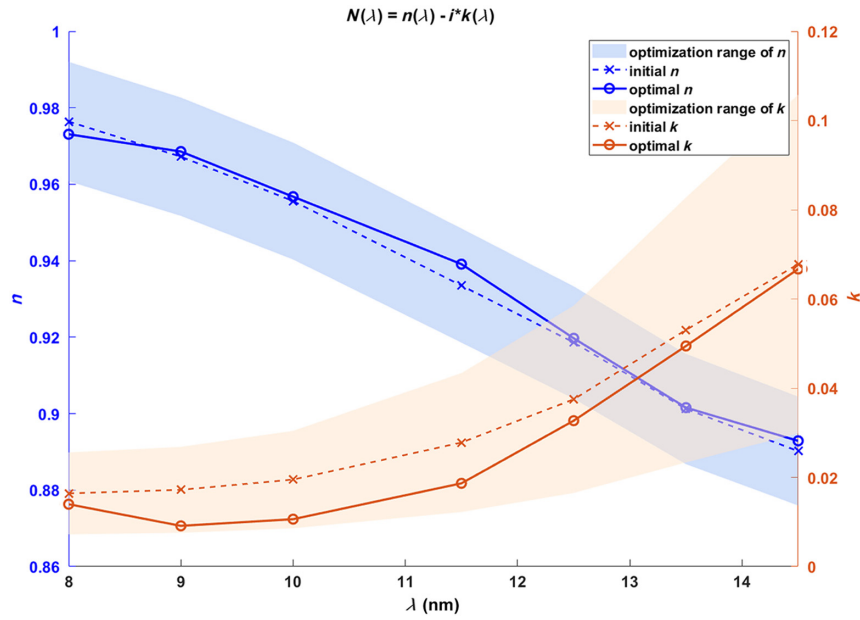


Fig. 6 Absorber n and k values versus wavelengths. Within the certain variation from the initial values, the optimal n and k are obtained by fitting our model to the experimental data, as shown in Fig. 7.

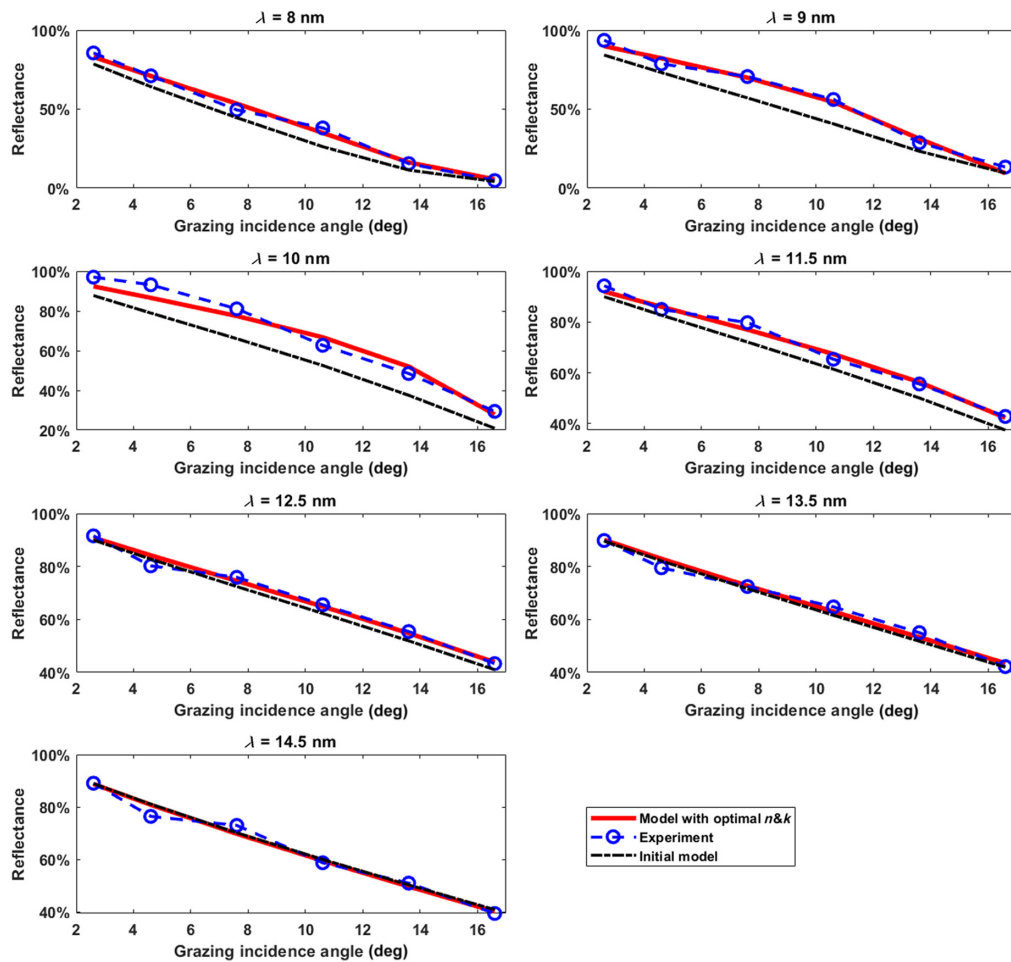


Fig. 7 Each subplot shows the reflectance as a function of the grazing angle of incidence for a specific wavelength. The reflectance curves refer to the initial model, to the experimental data, and to the model with optimized n and k values.

the thicknesses of absorber, Ru, and Ru_2Si_3 layers. We used the thickness uncertainties mentioned in Sec. 2.1 as the variation ranges in the direct-search optimization process to get the more accurate thicknesses. This ensures that the corresponding sample reflectance has the minimum RMS difference compared with the experimental results, as shown in Fig. 8. As a geometric

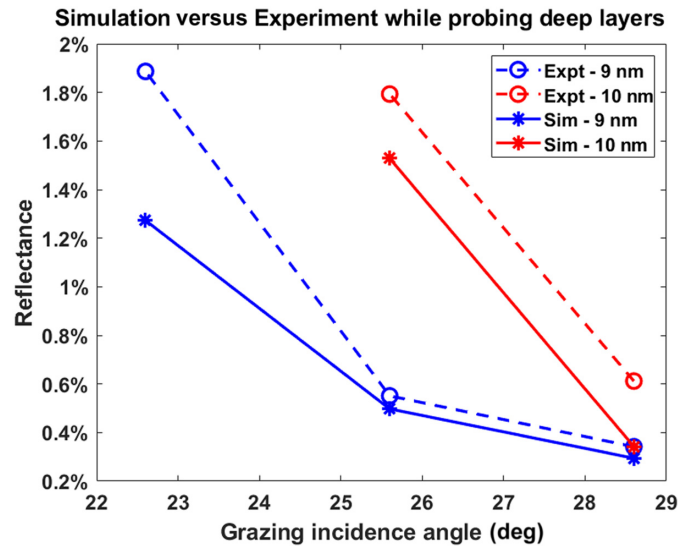


Fig. 8 Sample reflectance of experiment (Expt) versus simulation (Sim) with the optimal n and k values of absorber and optimal thicknesses of absorber, Ru, and Ru_2Si_3 .

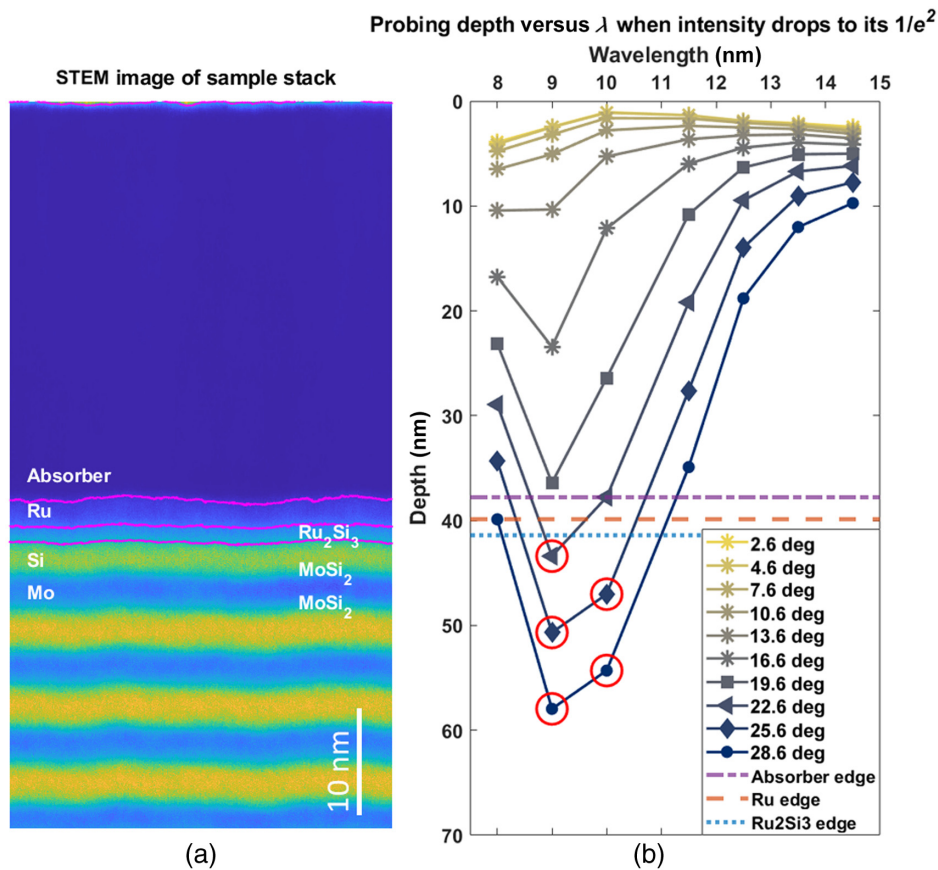


Fig. 9 (a) STEM image of few top layers of the sample stack. (b) The probing depth calculated with the characterized absorber n and k , as well as the characterized thicknesses of the absorber, Ru, and Ru_2Si_3 layers.

Table 1 Sample layer thickness summary.

Layer	Design (nm)	STEM (nm)	REGINE (nm)
Absorber	33	37.53 ± 0.25	37.7(6)
Ru	2.5	2.48 ± 0.37	2.1(2)
Ru_2Si_3	N/A	1.53 ± 0.38	1.5(1)
Si	4.2	1.86 ± 0.30	N/A
MoSi_2	N/A	1.69 ± 0.30	N/A
Mo	2.8	1.94 ± 0.28	N/A
MoSi_2	N/A	1.80 ± 0.29	N/A

property, the layer thickness is independent of the illumination wavelength, the RMS is calculated for all the data points in this figure, and not separately for each wavelength as we did before for the n and k characterization. Once we obtained the characterized thicknesses of the first three layers, we updated the sample model again and calculated the sample reflectance (Fig. 8) and probing depth [Fig. 9(b)].

Figure 9(a) shows the STEM image of the sample stack. The intermixing layers of Ru_2Si_3 and MoSi_2 are clearly visible. The magenta lines are the estimated edge profiles of the absorber, Ru, and Ru_2Si_3 layers, which were used to calculate the thicknesses in the initial sample model, as mentioned in Sec. 2.1. Figure 9(b) shows the beam probing depth with the sample model updated with the new n and k values and the characterized thicknesses of absorber, Ru, and Ru_2Si_3 layers. As there are only two data points below one period of the Si/Mo multilayer, we kept the thicknesses of Si, Mo, and MoSi_2 the same as analyzed in Fig. 2 and only optimized the thicknesses of the absorber, the Ru capping layer, and the Ru_2Si_3 intermixing layer in the simulation.

The comparison of the REGINE characterized layer thickness, the STEM measurement and the original design dimension is shown in Table 1. The absorber layer thickness has a 14.2% difference compared with the designed value, which was also confirmed by the STEM measurement. This difference most likely came from the inaccurate control of the deposition step in the sample fabrication process. The REGINE characterized Ru capping layer is slightly thinner than the designed and STEM values, which is due to the formation of the intermixing layer of Ru_2Si_3 while depositing the Ru on top of Si. Notably, REGINE is designed for grazing incidence sample analysis, and this sample would have been probed more efficiently with a close to normal illumination setup. Thus to perform a more meaningful analysis of the multilayer, we would need a sample without the absorber layer.

4 Conclusions

In this paper, we used the REGINE instrument's reflectometry capability to characterize the refractive index (n) and extinction coefficient (k) of an EUV attenuated phase-shifting photomask blank's absorber material. We measured the sample's reflectance experimentally using a spectral reflectometry approach at the grazing incidence angles less than 17 deg. Simultaneously, we constructed a model of the sample and computed its reflectance using the TMM. Then, we adjusted the refractive index (n) and extinction coefficient (k) values of the top layer (absorber) in the model until the calculated reflectance closely matched the experimental data. The accurate n and k values of the absorber material are then extracted from the model.

Furthermore, we showed how, by judiciously selecting the combination of illumination wavelength and grazing incidence angle, we were able to adjust the probing depth of REGINE, enabling the measurement of the thicknesses of the absorber layer, the Ru capping layer, and the previously undefined Ru_2Si_3 intermixing layer. With a new sample featuring a thinner absorber layer or without absorber, REGINE could probe even deeper, allowing inference of n and k values of the intermixing layers and layer thickness within the Si/Mo multilayer structure.

This versatility extends its application to the characterization of various parameters and opens avenues for investigating other thin films and stacked structures, which will further contribute to the research and development of alternative photomasks.

The results presented in this paper also highlight the potential of REGINE as a valuable tool in the semiconductor industry, providing metrology for photomask and patterned wafer manufacturing processes. Its ability to provide detailed material properties and layer thickness information positions it as a valuable asset in the development of smaller, faster, and more energy-efficient electronic devices through EUVL.

Disclosures

The authors declare no conflicts of interest.

Code and Data Availability

The code and data that support the findings of this study are available from the corresponding author upon request.

Acknowledgments

We thank Dr. Dimitrios Kazazis for fruitful discussions about the sample structure and STEM image analysis. We also thank Markus Kropf, Michaela Vockenhuber, and Renzo Rotundo for the technical supports of the REGINE setup development. We would like to thank the funding sources for this project, SAMSUNG Global Research Outreach Program (Grant No. IO230403-05730-01) and Swiss National Science Foundation (Grant Nos. IZKSZ2_188410 and 206021_177020). This paper is the detailed version of the spectral reflectometry part of a SPIE proceeding paper entitled “EUV reflectometry and scatterometry for thin layer and periodic structure characterization.” The SPIE proceeding paper was presented at the 2024 SPIE advanced lithography + patterning conference.

References

1. A. Pirati et al., “EUV lithography performance for manufacturing: status and outlook,” *Proc. SPIE* **9776**, 97760A (2016).
2. J. P. Benschop, “EUV lithography: past, present and future,” *Proc. SPIE* **11609**, 1160903 (2021).
3. J. Miyazaki and A. Yen, “EUV lithography technology for high-volume production of semiconductor devices,” *J. Photopolym. Sci. Technol.* **32**(2), 195–201 (2019).
4. A. C. Diebold, *Handbook of Silicon Semiconductor Metrology*, CRC Press (2001).
5. N. G. Orji et al., “Metrology for the next generation of semiconductor devices,” *Nat. Electron.* **1**(10), 532–547 (2018).
6. S. Sherwin, “Actinic EUV reflectometry and scatterometry: from national lab to commercial applications,” *Proc. SPIE* **12292**, 122921E (2022).
7. Y. Esashi et al., “Tabletop extreme ultraviolet reflectometer for quantitative nanoscale reflectometry, scatterometry, and imaging,” *Rev. Sci. Instrum.* **94**(12), 123705 (2023).
8. C. Porter et al., “Soft X-ray: novel metrology for 3D profilometry and device pitch overlay,” *Proc. SPIE* **12496**, 124961I (2023).
9. S. Doering et al., “EUV reflectometry for thickness and density determination of thin film coatings,” *Appl. Phys. A* **107**, 795–800 (2012).
10. M. G. Sertsu et al., “Analysis of buried interfaces in multilayer mirrors using grazing incidence extreme ultraviolet reflectometry near resonance edges,” *Appl. Opt.* **54**(35), 10351–10358 (2015).
11. R. Ciesielski et al., “Determination of optical constants of thin films in the EUV,” *Appl. Opt.* **61**(8), 2060–2078 (2022).
12. K. M. Dorney et al., “Actinic inspection of the EUV optical parameters of lithographic materials with lab-based radiometry and reflectometry,” *Proc. SPIE* **12494**, 1249407 (2023).
13. V. Soltwisch et al., “High-precision optical constant characterization of materials in the EUV spectral range: from large research facilities to laboratory-based instruments,” *Proc. SPIE* **12472**, 124720Q (2022).
14. T. Shen, Y. Ekinici, and I. Mochi, “Reflective grazing incidence EUV nanoscope for wafer metrology,” *Proc. SPIE* **12292**, 122920O (2022).
15. T. Shen et al., “EUV grazing-incidence lensless imaging wafer metrology,” *Proc. SPIE* **12496**, 124960Z (2023).
16. T. Shen et al., “EUV reflective coherent diffraction imaging system for wafer metrology,” *Proc. SPIE* **12618**, 126180N (2023).

17. J. Rodenburg and A. Maiden, "Ptychography," in *Springer Handbook of Microscopy*, P. W. Hawkes and John C. H. Spence, Eds., pp. 819–904, Springer (2019).
18. A. Tripathi, I. McNulty, and O. G. Shpyrko, "Ptychographic overlap constraint errors and the limits of their numerical recovery using conjugate gradient descent methods," *Opt. Express* **22**(2), 1452–1466 (2014).
19. Y. Kim et al., "Platinum-based alloy absorber with improved etching properties for next-generation EUV mask," *Proc. SPIE* **12750**, 127500R (2023).
20. A. Yakshin et al., "Determination of the layered structure in mo/si multilayers by grazing incidence X-ray reflectometry," *Phys. B: Condens. Matter* **283**(1–3), 143–148 (2000).
21. L. Pasquali et al., "Formation and distribution of compounds at the Ru–Si(001) ultrathin film interface," *J. Appl. Phys.* **105**(4), 044304 (2009).
22. B. L. Henke, E. M. Gullikson, and J. C. Davis, "X-ray interactions: photoabsorption, scattering, transmission, and reflection at $e = 50 - 30,000$ eV, $z = 1 - 92$," *At. Data Nucl. Data Tables* **54**(2), 181–342 (1993).
23. E. Hecht, *Optics*, 4th ed., Eugene Hecht Reading (2001).
24. M. Born and E. Wolf, *Principles of Optics: Electromagnetic THEORY of propagation, Interference and Diffraction of Light*, Elsevier (2013).
25. W. Swann, "Direct search methods," in *Numerical Methods for Unconstrained Optimization*, W. Murray, Ed., pp. 13–28, Academic Press, London/New York (1972).

Tao Shen is a doctoral student at Paul Scherrer Institute and ETH Zurich. He received his MS degree in optics and photonics from Karlsruhe Institute of Technology in 2019. His current research interests include semiconductor metrology, metrology instrumentation, and optical design. He is a student member of SPIE.

Iacopo Mochi is the leader of the Advanced Lithography and Metrology group at PSI. He started working on EUV mask inspection in 2008 at LBNL in the Center for X-Ray Optics, where he contributed to the development of the SHARP microscope. Later, he joined IMEC as an R&D engineer studying SRAF solutions to mitigate EUV mask 3D effects. Since 2016, he has been working on instrumentation development for EUV lithography and metrology at PSI.

Biographies of the other authors are not available.